Hindawi
Journal of Nanomaterials
Volume 2022, Article ID 6522007, 10 pages
https://doi.org/10.1155/2022/6522007

Research Article

Improvement of the Parameter Distribution of $TiN/HfO_2/CeO_x$/TiN Memristors by Rapid Thermal Annealing

Guihua Yao,[1] Zhaozhu Qu,[1] Changfang Li,[1] Yuntao Peng,[2] Qixin Li,[3] Zhaohui Zeng,[3] Jianghui Dong,[2] and Baolin Zhang[1]

[1]*Key Laboratory of New Processing Technology for Nonferrous Metal & Materials, Ministry of Education, Guangxi Key Laboratory of Optical and Electronic Materials and Devices, College of Materials Science and Engineering, Guilin University of Technology, Jian Gan Road 12, Guilin 541004, China*
[2]*Guangxi Engineering Research Center of Digital Medicine and Clinical Translation, College of Biotechnology, Guilin Medical University, Guilin 541004, China*
[3]*Institute of Semiconductors, Guangdong Academy of Sciences, Guangdong 510650, China*

Correspondence should be addressed to Jianghui Dong; djh1028@126.com and Baolin Zhang; baolinzhang@ymail.com

Received 22 December 2021; Revised 11 March 2022; Accepted 16 March 2022; Published 11 April 2022

Academic Editor: Mazeyar Parvinzadeh Gashti

Copyright © 2022 Guihua Yao et al. This is an open access article distributed under the Creative Commons Attribution License, which permits unrestricted use, distribution, and reproduction in any medium, provided the original work is properly cited.

$TiN/HfO_2/CeO_x/TiN$ memristors were prepared by magnetron sputtering. To further improve their performance, the devices were rapidly thermally annealed at different temperatures for different times. Compared with those of unannealed devices, the coefficients of variation (CVs) of the set voltage (V_{SET}) and the reset voltage (V_{RESET}) were reduced by 35.1% and 59.4%, respectively, and the CVs of the resistances in low and high resistance states (R_{LRS} and R_{HRS}) were reduced by 70.2% and 52.7%, respectively, after annealing at 400°C for 2 min in air. Through X-ray diffraction, X-ray photoelectron spectroscopy, and *I-V* curves of the devices before and after annealing, we propose that the combined effect of grain growth (i.e., grain boundary reduction) and decreased oxygen vacancy content in the switching film resulting from annealing is responsible for the improvement in the switching parameter distribution of $TiN/HfO_2/CeO_x/TiN$ devices. This work presents a simple way to enhance the performance of memristors.

1. Introduction

Memristors have great potential as next-generation memory devices because of their high scalability, simple structure, rapid resistance switching and compatibility with CMOS technology [1–4]. In general, the resistance switching mechanism of memristors relies on the formation/disruption of conductive filaments (CFs) resulting from oxygen vacancy or oxygen ion movements in oxide layers, and on the interface effects between electrodes and oxides [5–7]. Although the formation of CFs after activation by electroforming and resistance switching has been observed [8] and quantitative information (diameter, composition, and gap width) of CFs has been investigated [9], the formation/disruption of CFs in the oxide layer still needs further elucidation and adjustment. Oxygen vacancies can reduce the bandgap and enhance the conductivity of oxide materials, leading to the formation of CFs [10, 11]. The intrinsic conductivity of oxide materials leads to different electrical activation modes, such as field-induced electroforming and current bifurcation-induced electroforming [12], which affect the switching characteristics of memristors. At the same time, because of the variation in or nonuniform structure of resistive switching materials [13, 14], the resistances of memristor devices in high/low resistance (R_{HRS}/R_{LRS}) states vary greatly, which restricts their further development and application. The fundamental causes of variations in memristors parameters and the methods to improve these properties need to be further studied [15].

Ceria has been studied as a switching material for memristors [1, 2, 16–18]. Its excellent oxygen storage/release capacity is because the two most common cation valence

states, Ce^{4+} and Ce^{3+}, are prone to redox reactions [19–21]. However, memristors based on CeO_x still have severe problems, such as high switching parameter dispersion and high operating current. Annealing can decrease the number of defects and improve the crystal quality of films. It has been reported that proper annealing can improve the switching endurance, on/off ratio, data retention and uniformity in the operational parameters of memristors [16, 22]. However, there is still no insight into the reasons why annealing improves the resistance switching properties. In this study, TiN/HfO_2/CeO_x/TiN memristors were prepared. A HfO_2 layer was used to increase the initial resistances of CeO_x-based memristor devices and to modulate the separation and recombination of oxygen ions/vacancies during resistance switching [7]. The effects of annealing the devices at different temperatures and times on the characteristics of resistive switching were studied. The stability of the switching parameters of TiN/HfO_2/CeO_x/TiN was obviously improved after annealing at 400°C for 2 min. We propose that the combined effect of grain growth and decrease in oxygen vacancy content accounts for this improvement. This work shows that annealing can be a general and effective way to reduce the dispersion of memristor switching parameters.

2. Experiment

2.1. Materials. A TiN target was used to deposit a 100 nm thick TiN bottom electrode (BE) on SiO_2 (300 nm)/Si (450 μm) substrates by direct current (DC) sputtering with a sputtering time of 2000 s, a sputtering atmosphere of 10% N_2, and a sputtering power of 150 W. Next, a CeO_2 target was used to deposit a 30 nm thickness CeO_x layer by radio frequency (RF) sputtering for 4000 s in an atmosphere with an Ar : O_2flow rate ratio = 11.2 sccm : 5.6 sccm with a sputtering power of 80 W. Then, a HfO_2 target was used to deposit a 10 nm thick HfO_2 layer by RF sputtering (100 W) for 300 s in 16.8 sccm Ar. Finally, TiN with a thickness of 100 nm and diameter of 50 μm was deposited as the top electrode (TE) by DC sputtering and was patterned by ultraviolet lithography to expose the AZ4620 photoresist-coated wafer. TiN/HfO_2/CeO_x/TiN devices were obtained. Some of the TiN/HfO_2/CeO_x/TiN were rapidly thermally annealed in air at different temperatures (200 to 400°C) for different times (2 to 20 min).

2.2. Characterization. Scanning electron microscopy (SEM, Hitachi S-4800), X-ray diffraction (XRD, SmartLab Mini flex600) and X-ray photoelectron spectroscopy (XPS, ESCALAB 250Xi) were utilized to investigate the cross-section morphology, chemical composition, and crystal structure of CeO_x and HfO_2. For XRD, a 0.5° grazing angle, 1 divergence slit, and 20°–80° scanning angles were adopted. For XPS, Avantage software was used to analyze the data, and the binding energy scale was calibrated with the C 1s peak at 284.8 eV.

A Keithley 4200-SCS analyzer was used to measure the electrical properties of all devices. Bias voltages were applied to the TiN TE, the TiN BE was grounded during electrical property measurements, and the sweep rate was 0.01 V/step. All tests for electrical property determination were performed at room temperature.

3. Results

3.1. SEM Analyses of TiN/HfO_2/CeO_x/TiN. Figure 1(a) shows the structural diagrams of TiN/HfO_2/CeO_x/TiN. Figure 1(b) shows the morphology of the cross-section of the devices. The layers of the different compounds with uniform thicknesses are clearly shown. The thickness of each layer realized by the magnetron sputtering parameters is in accordance with the design.

3.2. I-V Curves of Annealed and Unannealed TiN/HfO_2/CeO_x/TiN Devices. The forming voltages of TiN/HfO_2/CeO_x/TiN before annealing were 8.83 ± 0.70 V (the average results of 16 devices) with a compliance current of 1 mA. After forming the devices were switched from the LRS (low resistance state) to the HRS (high resistance state) and vice versa with voltage sweeping from 0 to ±2 V (Figure 2(a)). The forming voltages of TiN/HfO_2/CeO_x/TiN after annealing at 400°C for 2 min were 8.63 ± 0.70 V (the average results of 16 devices) with a compliance current of 1 mA. After forming the devices were switched from the LRS to the HRS and vice versa with voltage sweeping from 0 to ±2 V (Figure 2(b)). The cumulative distributions of the V_{SET} (set voltage), V_{RESET} (reset voltage), R_{LRS}, and R_{HRS} of TiN/HfO_2/CeO_x/TiN devices before and after annealing at 400°C for 2 min are shown in Figures 2(c) and 2(d). Table 1 shows that the dispersions of the V_{SET}, V_{RESET}, R_{LRS}, and R_{HRS} of the annealed devices were significantly less than those of the devices before annealing. The coefficients of variation (CV = standard deviation/mean value) of V_{SET} decreased from 15.68% to 10.18% (a decrease of 35.1%), and the CVs of V_{RESET} decreased from 4.56% to 1.85% (a decrease of 59.4%). For TiN/HfO_2/CeO_x/TiN, the CVs of R_{LRS} decreased from 36.95% before annealing to 10.99% after annealing (a decrease of 70.2%), and the CVs of R_{HRS} decreased from 47.56% before annealing to 22.48% after annealing (a decrease of 52.7%).

The current-voltage (*I*-*V*) curves of TiN/HfO_2/CeO_x/TiN annealed at different annealing temperatures and times with voltage sweeping from 0 V to ±5 V to 0 V (forming was not applied) are shown in Figure 3. The conductance of the devices increased with increasing annealing temperature and time. However, with increasing annealing time, the relative conductance of the annealed devices decreased (but was still higher than that of the unannealed devices). The conductance changes may be caused by the combined effect of the oxygen vacancy concentration and microstructure of the films modified by annealing, and we will clarify this in the discussion section.

3.3. XRD and Grain Size Analyses of Unannealed and Annealed TiN/HfO_2/CeO_x/TiN. Figure 4 shows the XRD patterns of TiN/HfO_2/CeO_x/TiN and the change in grain sizes of CeO_x thin films at different annealing temperatures and times. From Figure 4(a), the (103) and (121) diffraction peaks show the HfO_2 orthorhombic crystal structure

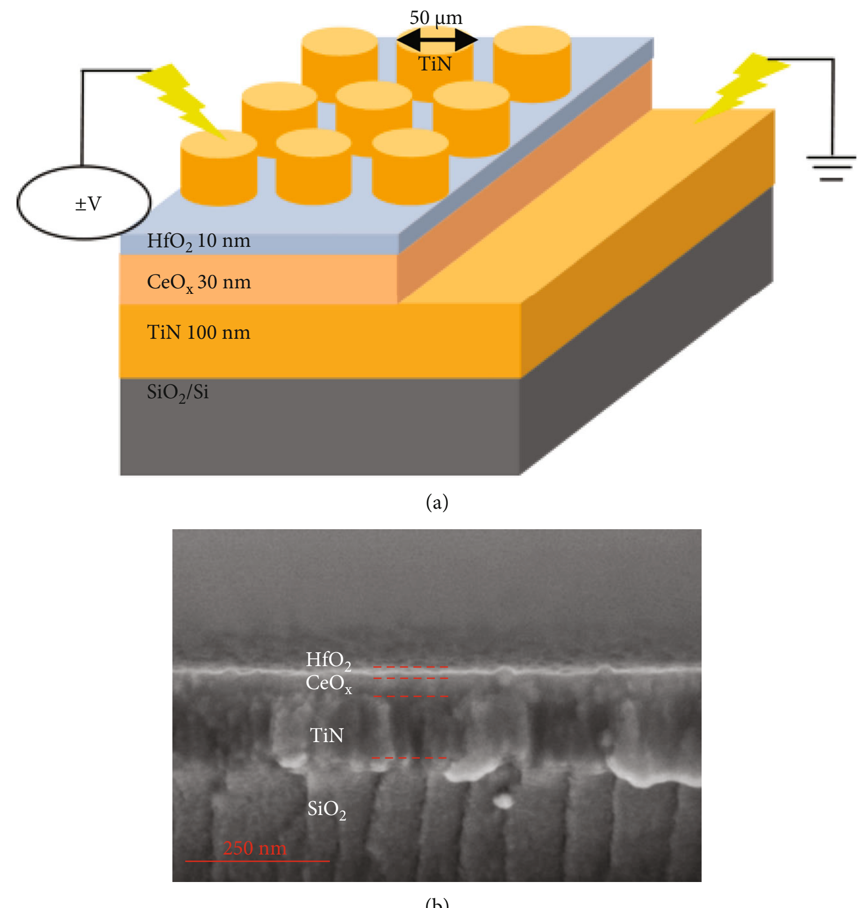

FIGURE 1: (a) Schematic diagram of TiN/HfO_2/CeO_x/TiN. (b) SEM image of the cross section of TiN/HfO_2/CeO_x/TiN.

(JCPDS#40-1173), and (111) the diffraction peaks show the CeO_x cubic crystal structure (JCPDS#34-0394). With increasing annealing temperature and time (Figures 4(a) and 4(b)), the CeO_2 (111) diffraction peak intensity gradually increases, and the diffraction peaks of CeO_2 (220) and CeO_2 (311) appear and gradually grow. All the diffraction peak intensities of CeO_x gradually increased, and the full width at half maximum (FWHM) of the peaks decreased. However, the diffraction peaks of CeO_x annealed for 5 min, 10 min, and 20 min did not change obviously.

According to the Scherrer formula [23], $D = k\gamma/Bcos\theta$ (B is the FWHM, D is the grain size, K is the Scherrer constant, θ is the Bragg diffraction angle, and γ is the X-ray wavelength), we calculated the grain sizes from the FWHM of CeO_2 (111) peaks for the CeO_x films, as shown in Figure 4(c). The CeO_x grain sizes increased with increasing annealing temperature. However, the CeO_x grain sizes almost did not change with increasing annealing time. No obvious grain growth of HfO_2 was observed from the calculation according to the Scherrer formula. From these results, we speculated that the decrease in the R_{LRS} and R_{HRS} dispersions of TiN/HfO_2/CeO_x/TiN devices after annealing (400°C, 2 min) may be related to the increase in CeO_x grain sizes.

3.4. Oxygen Vacancy Concentrations in TiN/HfO_2/CeO_x/TiN Analyzed by XPS. The analysis depth of XPS analyses was 2–5 nm, and the region that was not covered with the top TiN electrode was focused on by an electron beam to analyze the O 1s signals of the HfO_2 films under different annealing conditions. Figures 5(a) and 5(b) show the XPS spectra of the Hf 4f and Ce 3d peaks of TiN/HfO_2/CeO_x/TiN (unannealed). The binding energies of 16.58 eV (Hf 4f7) and 18.18 eV (Hf 4f5) correspond to the Hf^{4+} oxidation state. The binding energies of 882.58 eV, 889.08 eV, 898.48 eV, 901.08 eV, 907.08 eV, and 916.48 eV correspond to the Ce^{4+} oxidation state. The binding energies of 885.68 eV and 903.68 eV correspond to the Ce^{3+} oxidation state. The O 1s XPS peak at 529.98 eV (Figure 5(c)) of the HfO_2 films under different annealing conditions is ascribed to lattice oxygen in HfO_2, and the O 1s peak at 531.88 eV is ascribed to nonlattice oxygen, as reported in the literature [24, 25]. The oxygen vacancy concentration is proportional to the ratio of the nonlattice oxygen concentration [26], so nonlattice oxygen concentration can be used to qualitatively analyze the oxygen vacancy concentration. The oxygen vacancy concentration percentages are calculated by the areas below the peaks, which are adjusted by sensitivity factors [27]. Figures 5(d) and 5(e) show the oxygen vacancy concentrations in HfO_2 films annealed in air at different temperatures and times. With increasing annealing temperature and time, the oxygen vacancy concentration in the HfO_2 films decreased.

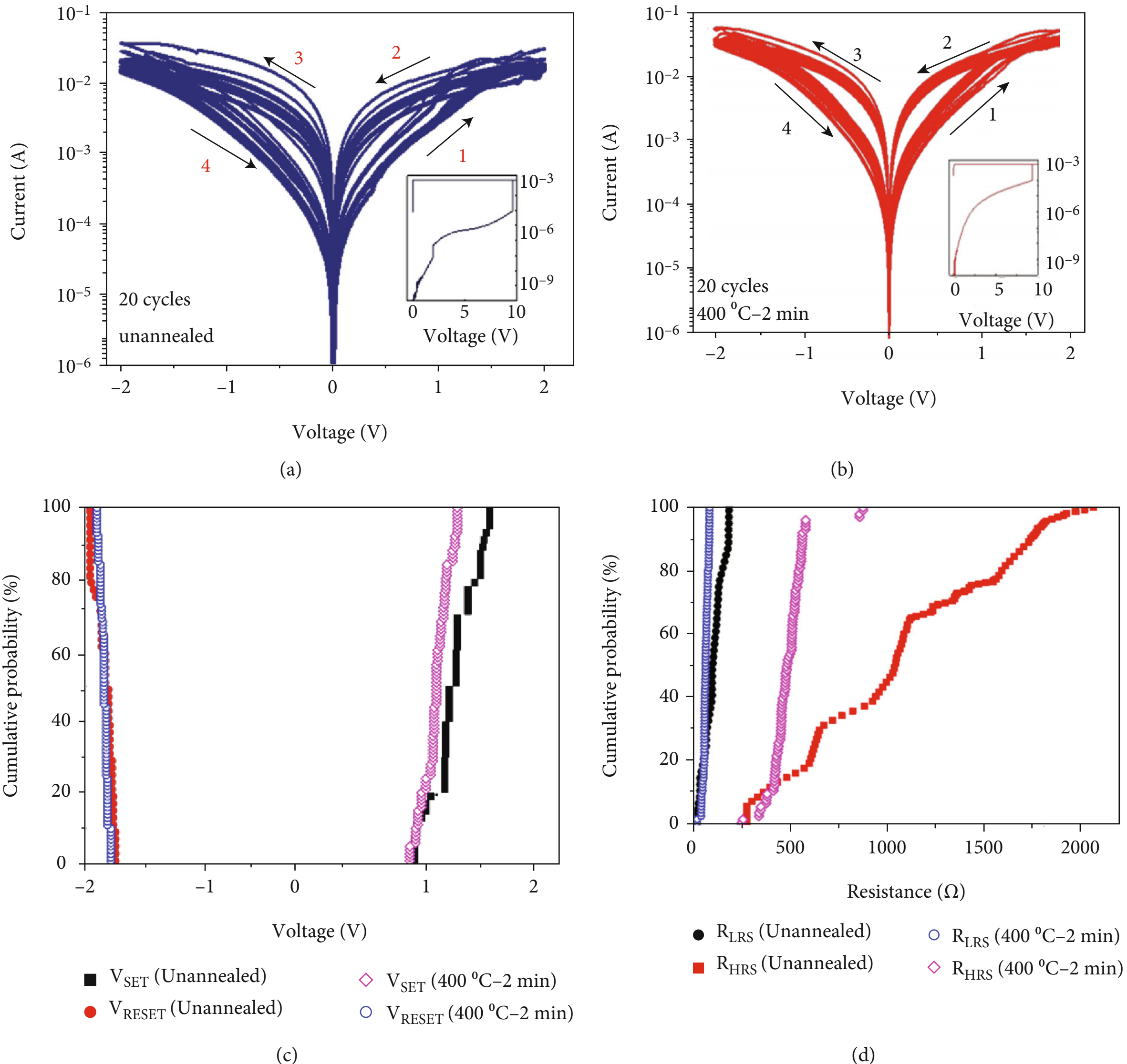

Figure 2: *I-V* curves of unannealed TiN/HfO_2/CeO_x/TiN devices (a) and annealed TiN/HfO_2/CeO_x/TiN devices (b) with voltage sweeping from 1 ⟶ 2 and 3 ⟶ 4 and cumulative probabilities of the V_{SET} and V_{RESET} (c) and R_{HRS} and R_{LRS} (d) of TiN/HfO_2/CeO_x/TiN, after the forming process (the insets show the forming process).

Table 1: Mean values, standard deviation, and CV* (in the brackets) of the V_{SET}, V_{RESET}, R_{LRS}, and R_{HRS} of TiN/HfO_2/CeO_x/TiN devices before and after annealing at 400°C for 2 min.

	V_{SET} (V) [CV]	V_{RESET} (V) [CV]	R_{LRS} (Ω) [CV]	R_{HRS} (Ω) [CV]
TiN/HfO_2/CeO_x/TiN (unannealed)	1.19 ± 0.18 [15.68%]	−1.82 ± 0.08 [4.56%]	129.56 ± 47.87 [36.95%]	1100.04 ± 523.19 [47.56%]
TiN/HfO_2/CeO_x/TiN (400°C-2 min)	1.05 ± 0.11 [10.18%]	−1.82 ± 0.03 [1.85%]	93.57 ± 10.28 [10.99%]	521.70 ± 117.3 [22.48%]

*CV (coefficient of variation) = standard deviation/mean value.

Annealing in air can also remarkably reduce the oxygen vacancy concentration in CeO_x, which has been proven in our previous work [28]. After annealing in an air atmosphere, the Ce^{3+}in CeO_x lost an electron and was oxidized to Ce^{4+}, which was accompanied by the elimination of oxygen vacancies. With increasing annealing temperature and time, the oxygen vacancy concentration in CeO_x films decreased.

4. Discussion

4.1. The Conduction Mechanism Fitting of TiN/HfO_2/CeO_x/TiN. To elucidate the resistive switching behavior of TiN/HfO_2/CeO_x/TiN, the *I-V* curves of the devices were fitted with conductive mechanisms (Figures 6(a) and 6(b)). When the unannealed and annealed devices were in the HRS (the

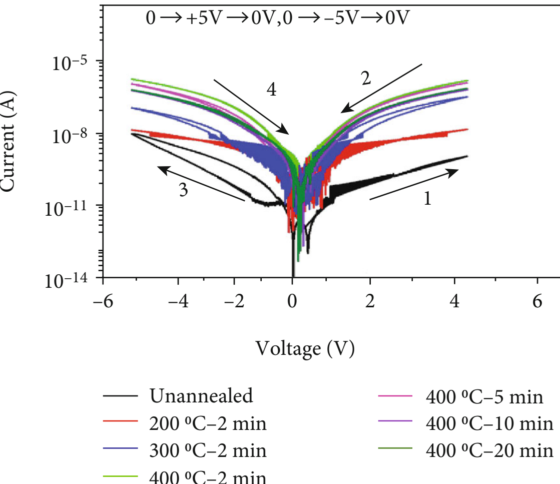

FIGURE 3: *I-V* curves of TiN/HfO_2/CeO_x/TiN devices with voltage sweeping from 0 V to ±5 V to 0 V (forming was not applied) at different annealing temperatures and times.

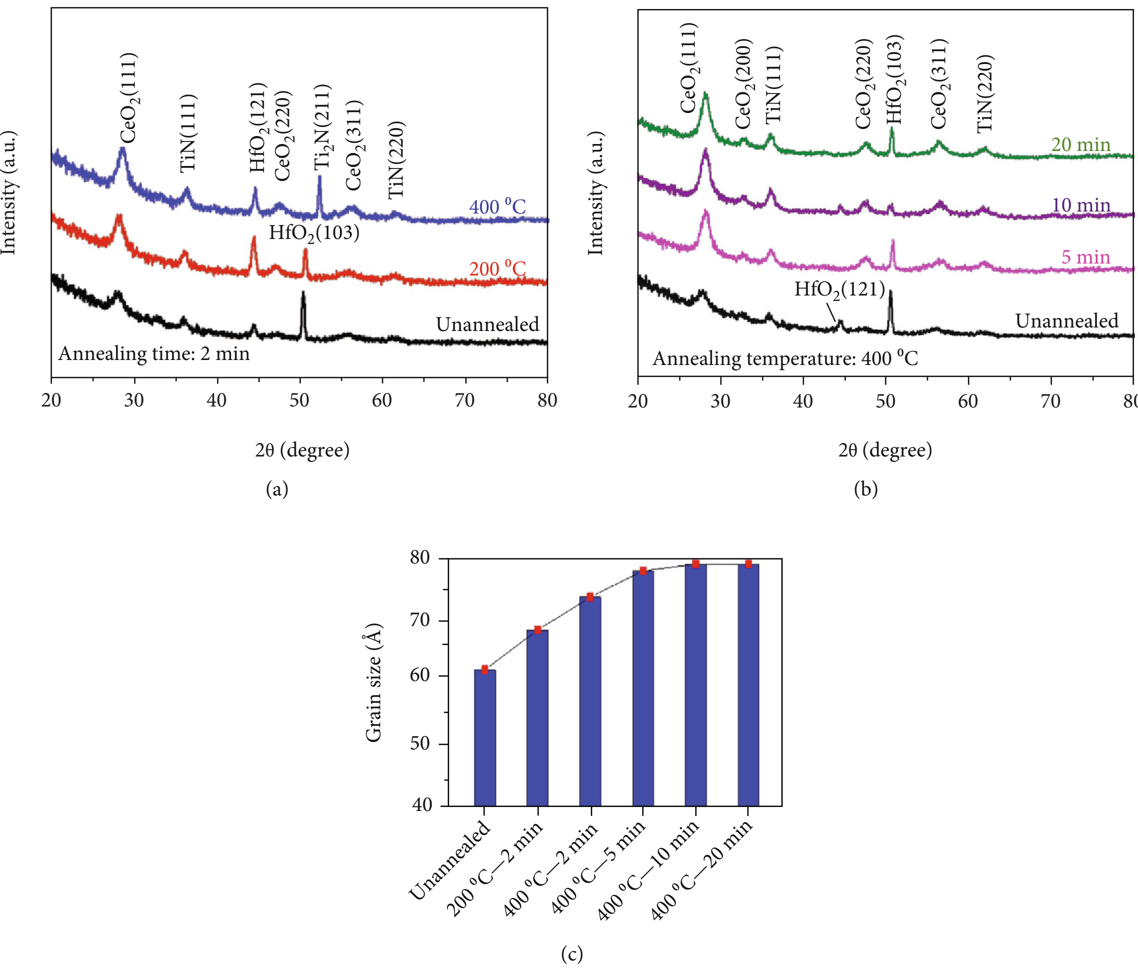

FIGURE 4: Small-angle grazing incidence XRD patterns of TiN/HfO_2/CeO_x/TiN at different annealing temperatures (annealing time: 2 min) (a) and with different annealing times (annealing temperature: 400°C) (b). CeO_x grain size changes under different annealing conditions (c).

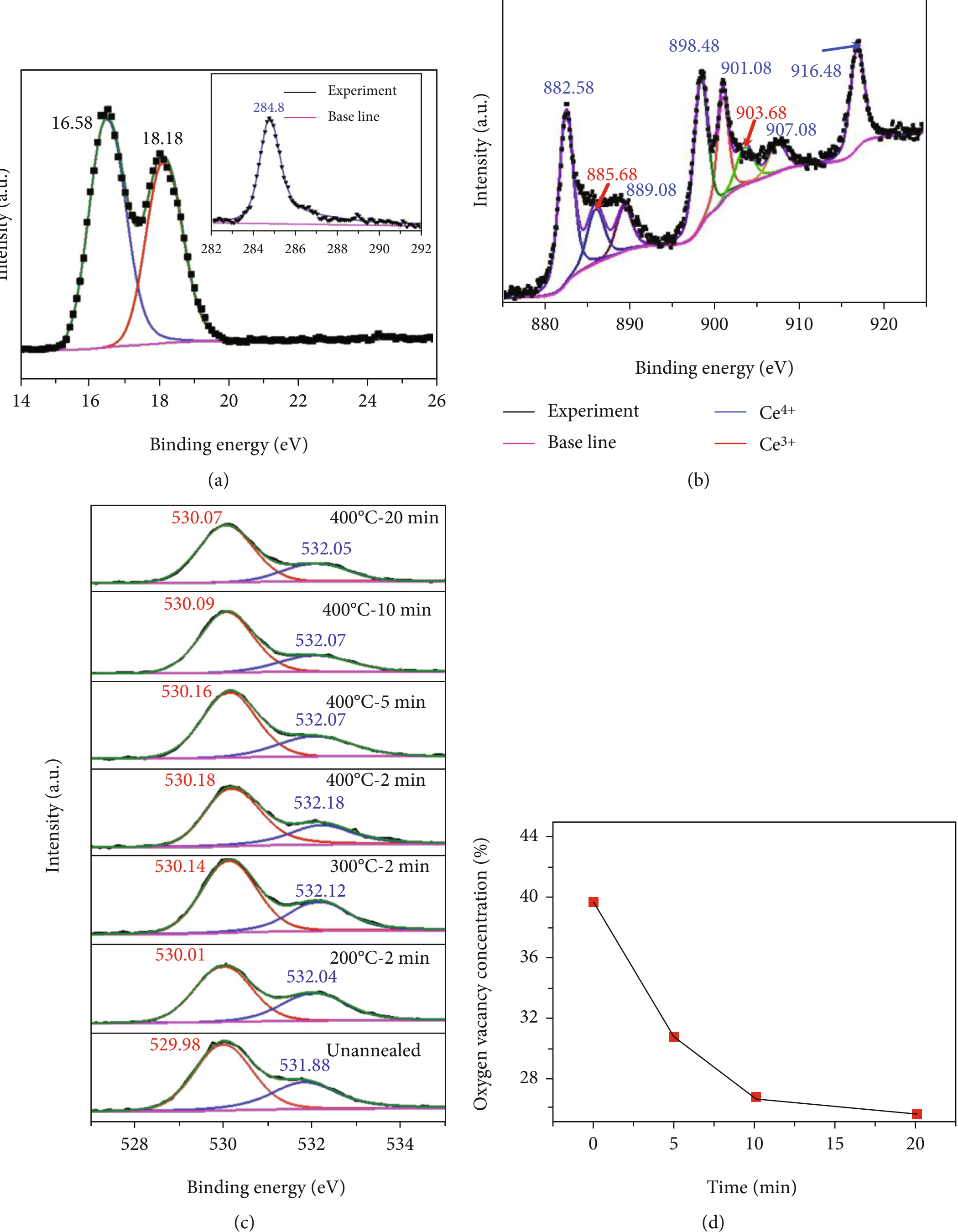

Figure 5: Continued.

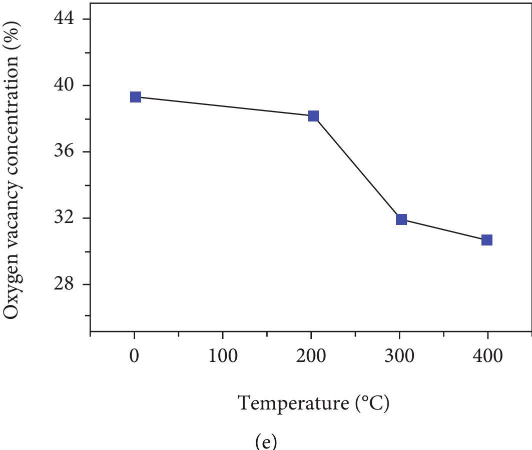

(e)

Figure 5: XPS spectra showing the Hf 4f peaks (a) (the inset shows the C 1s peak at 284.8 eV for calibration) and Ce 3d peaks (b) of TiN/HfO_2/CeO_x/TiN (unannealed). XPS spectra showing the O 1s peaks for the HfO_2 films of TiN/HfO_2/CeO_x/TiN under different annealing conditions (c). Change in the oxygen vacancy concentration of the HfO_2 films after annealing at 400°C for different times (d) and after annealing at different temperatures for 2 min (e).

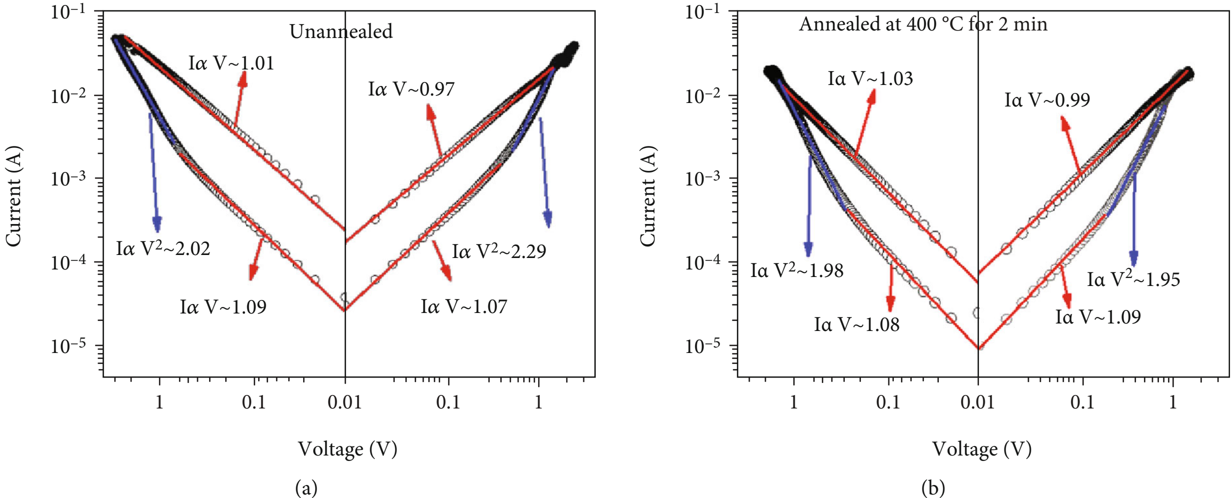

Figure 6: Log-log I-V curves and their fit for determining the conduction mechanism of the unannealed TiN/HfO_2/CeO_x/TiN devices (a) and TiN/HfO_2/CeO_x/TiN devices annealed at 400°C for 2 min (b).

lower curves in Figures 6(a) and 6(b)), the I-V curves possess linear parts with a slope of ~1, which indicates Ohmic conduction ($I \propto V$) [29] due to the partial filling of traps during the weak injection of charge carriers from the bottom/top TiN electrode; the I-V curves also possess rapid increasing current parts with a slope of ~2, which indicates Child's square law ($I \propto V^2$) [30] due to the injected electrons with applied bias which are trapped/detrapped in the CeO_x layer. These results suggest that the devices mainly followed the SCLC conduction mechanism in the HRS. When the unannealed and annealed devices are in the LRS (the upper parts of the curve in Figures 6(a) and 6(b)), the I-V curves are linear with slopes of ~1, implying that the conduction filament is the main conduction mechanism for the devices at the LRS. These results imply that the conduction mechanisms of TiN/HfO_2/CeO_x/TiN in the HRS and LRS did not changed after annealing.

4.2. Effect of Annealing on the Resistance Switching Characteristics of TiN/HfO_2/CeO_x/TiN. The conduction of CeO_x switching materials is composed of ionic conduction and electronic conduction [31]; both ionic conduction and electronic conduction are influenced by grain size (and, therefore, grain boundaries), and oxygen vacancies and their distribution. The preferential accumulation of oxygen vacancies along the grain boundary sites has been reported [32]. It was suggested that although there were oxygen vacancies in the grains, the oxygen vacancy concentration near the grain boundaries was generally higher than that in the inner grains, and furthermore, the oxygen vacancies in the grains were generally in linear but discontinuous arrangements, making it difficult to form a conduction channel in the grains. On the other hand, it was more likely that oxygen vacancies formed chains at the grain boundaries to construct the ionic conduction channel, and electrons also

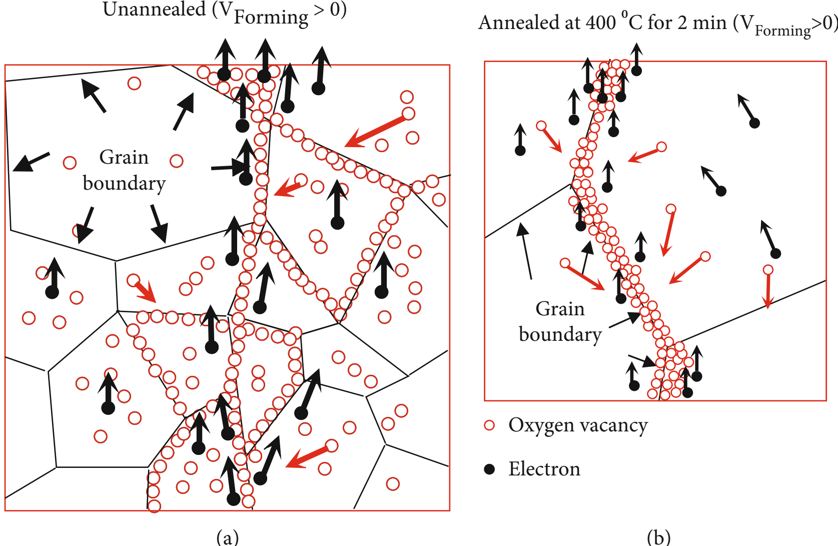

FIGURE 7: Possible conduction paths in the CeO_x of TiN/HfO_2/CeO_x/TiN before annealing (a) and after annealing at 400°C for 2 min (b).

tended to accumulate in the vicinity of the grain boundaries and hop along the oxygen vacancies to contribute to the conductivity [33].

In this work, annealing significantly reduced the dispersion of the V_{SET} and V_{RESET} and R_{LRS} and R_{HRS} of TiN/HfO_2/CeO_x/TiN devices (Table 1, Figures 2(c) and 2(d)), which could be ascribed to the combined effect of the increased grain size in the CeO_x films (no obvious grain size change was observed in HfO_2) (Figure 4(c)) and the reduced oxygen vacancy concentration in the HfO_2 and CeO_x films caused by annealing (Figure 5). Figure 7 clarifies the possible conduction paths in the CeO_x of TiN/HfO_2/CeO_x/TiN. It can be speculated that the oxygen vacancies accumulate along CeO_x grain boundaries, and that the oxygen vacancy channel forms and ruptures along the grain boundaries. For the unannealed devices, the channel forms and ruptures at more abundant boundaries (Figure 7(a)), while for the annealed devices the channel forms and ruptures at fewer positions because of the reduction in the number of grain boundaries (Figure 7(b)), and smaller variations in the conduction paths result in decreased dispersions of the V_{SET} and V_{RESET} and R_{LRS} and R_{HRS} of the annealed devices.

To support our proposition that the grain size (and, therefore, grain boundaries) and oxygen vacancy content jointly influence the conduction of the TiN/HfO_2/CeO_x/TiN devices, we measured the conductance of the devices before forming. The conductance in the HRS increased with increasing annealing temperature and time, as shown in Figure 3. Rapid thermal annealing at first results in grain growth (and, therefore, grain boundary reduction), which makes the oxygen vacancies that act as ion carriers [31] redistribute and concentrate in the new grain boundaries, tending to form a broad oxygen vacancy channel that facilitates ionic/electronic conductivity, resulting in an increase in conductivity in this regime. However, the relative conductance of the devices decreased with a further increase in annealing time. It can be speculated that the major factor influencing conductance is the oxygen vacancy concentration in this regime, because with the increase in annealing time, the grain size of the CeO_x films did not change much (Figure 4(c)), while the oxygen vacancy concentration decreased continually (Figures 5(d) and 5(e)), so the conductance of the devices with voltage sweeping from 0 V to ±5 V to 0 V decreased in this regime.

In addition, the interface effect might also be considered [34–36]. It was reported that the resistance of the HRS would decrease after annealing when a metal with high oxygen affinity was used as the TE [37], which is consistent with our result (Table 1). Moreover, the roughness between CeO_x/TiN interfaces increased with increasing grain size, which would enhance the uneven distribution of the local electric field to a certain extent, enhance the electric field intensity [38], and promote the formation of CFs. These combined effects might contribute to the reduction of the V_{SET} and V_{RESET} of the device and the dispersion of V_{SET} and V_{RESET}.

5. Conclusions

This work demonstrates that rapid thermal annealing can significantly reduce the coefficients of variation (CVs) of the V_{SET}, V_{RESET}, R_{LRS}, and R_{HRS} of TiN/HfO_2/CeO_x/TiN devices. Annealing increased the grain size and reduced the oxygen vacancy concentration of the switching layers of the devices. We suggest that the combined effect of grain size growth and oxygen vacancy reduction and redistribution is responsible for the improvement in the distributions of the V_{SET}, V_{RESET}, R_{LRS}, and R_{HRS} of annealed devices. This work shows the potential of rapid thermal annealing in optimizing the performance of memristive devices.

Data Availability

The data used to support the findings of this study are included within the article.

Conflicts of Interest

The authors declare that they have no conflicts of interest.

Authors' Contributions

Guihua Yao was responsible for investigation, writing the original draft, and review and editing. Baolin Zhang was responsible for conceptualization, supervision, writing the original draft, and review and editing. Zhaozhu Qu and Changfang Li were responsible for methodology and formal analysis. Yuntao Peng was responsible for formal analysis and review and editing. Qixin Li and Zhaohui Zeng were responsible for data curation and formal analysis. Jianghui Dong was responsible for conceptualization, supervision, writing the original draft, and review and editing.

Acknowledgments

This work was supported by the National Natural Science Foundation of China (52162022, 62061012), Guangxi Natural Science Foundation (2021JJA160015), Guangxi Scholar Grant (30501020001), Guilin Innovation Platform and Talents Program (2020010702 and 2020010703), Research and Innovation Base for Basic and Clinical Application of Nerve Injury and Repair (ZY21195042), Improving the Basic Ability ofYoung and Middle-aged University Teachers in Guangxi (No. 2020KY06015), Open Fund of Key Laboratory of New Processing Technology for Nonferrous Metal & Materials, Guilin University of Technology, Ministry of Education (19AA-1, 20KF-29), Research and Innovation Base for Basic and Clinical Application of Nerve Injury and Repair (ZY21195042), and Improving the Basic Ability of Young and Middle-aged University Teachers in Guangxi (No. 2020KY06015).

References

[1] Q. Hu, T. S. Kang, H. Abbas et al., "Resistive switching characteristics of Ag/MnO/CeO_2/Pt heterostructures memory devices," *Microelectronic Engineering*, vol. 189, pp. 28–32, 2018.

[2] M. Ismail, I. Talib, C.-Y. Huang et al., "Resistive switching characteristics of Pt/CeO_x/TiN memory device," *Japanese Journal of Applied Physics*, vol. 53, no. 6, article 060303, 2014.

[3] L. Hu, S. Zhu, Q. Wei et al., "Enhancement of resistive switching ratio induced by competing interfacial oxygen diffusion in tantalum oxide based memories with metal nitride electrode," *Applied Physics Letters*, vol. 113, no. 4, article 043503, 2018.

[4] S. Fatima, X. Bin, M. A. Mohammad, D. Akinwande, and S. Rizwan, "Graphene and MXene based free-standing carbon memristors for flexible 2D memory applications," *Advanced Electronic Materials*, vol. 8, no. 1, p. 2100549, 2022.

[5] U. Celano, L. Goux, R. De Graeve et al., "Imaging the three-dimensional conductive channel in filamentary-based oxide resistive switching memory," *Nano Letters*, vol. 15, no. 12, pp. 7970–7975, 2015.

[6] J. Sun, C. H. Jia, G. Q. Li, and W. F. Zhang, "Control of normal and abnormal bipolar resistive switching by interface junction on In/Nb:SrTiO3 interface," *Applied Physics Letters*, vol. 101, no. 13, p. 133506, 2012.

[7] J.-H. Ryu, C. Mahata, and S. Kim, "Long-term and short-term plasticity of Ta_2O_5/HfO_2 memristor for hardware neuromorphic application," *Journal of Alloys and Compounds*, vol. 850, p. 156675, 2021.

[8] S. Kumar, Z. Wang, X. Huang et al., "Conduction channel formation and dissolution due to oxygen thermophoresis/diffusion in hafnium oxide memristors," *ACS Nano*, vol. 10, no. 12, pp. 11205–11210, 2016.

[9] Y. Ma, J. M. Goodwill, D. Li et al., "Stable metallic enrichment in conductive filaments in TaO_x-based resistive switches arising from competing diffusive fluxes," *Advanced Electronic Materials*, vol. 5, no. 7, p. 1800954, 2019.

[10] J. Fatheema, S. Fatima, B. J. Ali et al., "Resistive switching in Al_2O_3 based trilayer structure with varying parameters via experimentation and computation," *AIP Advances*, vol. 10, no. 11, article 115218, 2020.

[11] J. Fatheema, T. Shahid, M. A. Mohammad et al., "A comprehensive investigation of MoO_3 based resistive random access memory," *RSC Advances*, vol. 10, no. 33, pp. 19337–19345, 2020.

[12] S. K. Nandi, S. K. Nath, A. E. El-Helou et al., "Electric field- and current-induced electroforming modes in NbO_x," *ACS Applied Materials & Interfaces*, vol. 12, no. 7, pp. 8422–8428, 2020.

[13] K.-J. Lee, L.-W. Wang, T.-K. Chiang, and Y.-H. Wang, "Effects of electrodes on the switching behavior of strontium titanate nickelate resistive random access memory," *Materials*, vol. 8, no. 10, pp. 7191–7198, 2015.

[14] A. M. Rana, T. Akbar, M. Ismail et al., "Endurance and cycle-to-cycle uniformity improvement in tri-layered CeO_2/Ti/CeO_2 resistive switching devices by changing top electrode material," *Scientific Reports*, vol. 7, no. 1, article 39539, 2017.

[15] M. Ismail, I. Talib, A. M. Rana et al., "Effect of bilayer CeO_{2-x}/ZnO and ZnO/CeO_{2-x} heterostructures and electroforming polarity on switching properties of non-volatile memory," *Nanoscale Research Letters*, vol. 13, no. 1, p. 318, 2018.

[16] M. Ismail, S. A. Khan, M. K. Rahmani et al., "Oxygen annealing effect on resistive switching characteristics of multilayer CeO_2/Al/CeO_2 resistive random-access memory," *Materials Research Express*, vol. 7, no. 1, article 016307, 2020.

[17] H. J. Kim, H. Zheng, J.-S. Park et al., "Artificial synaptic characteristics with strong analog memristive switching in a Pt/CeO_2/Pt structure," *Nanotechnology*, vol. 28, no. 28, article 285203, 2017.

[18] M. Ismail, M. W. Abbas, A. M. Rana et al., "Bipolar tri-state resistive switching characteristics in Ti/CeO_x/Pt memory device," *Chinese Physics B*, vol. 23, no. 12, article 126101, 2014.

[19] M. Ismail, C.-Y. Huang, D. Panda et al., "Forming-free bipolar resistive switching in nonstoichiometric ceria films," *Nanoscale Research Letters*, vol. 9, no. 1, pp. 1–8, 2014.

[20] M. Ismail, I. Talib, A. M. Rana, E. Ahmed, and M. Y. Nadeem, "Performance stability and functional reliability in bipolar resistive switching of bilayer ceria based resistive random access memory devices," *Journal of Applied Physics*, vol. 117, no. 8, article 084502, 2015.

[21] Z. G. Long, C. P. Zheng, and J. C. Li, "Enhanced resistive switching performance in rare-earth/high-κ CeO_2/ZrO_2 nanocomposite films," *Physics Letters A*, vol. 386, article 126995, 2021.

[22] D. Panda, C.-Y. Huang, and T.-Y. Tseng, "Resistive switching characteristics of nickel silicide layer embedded HfO_2 film," *Applied Physics Letters*, vol. 100, no. 11, p. 112901, 2012.

[23] A. L. Patterson, "The Scherrer formula for X-ray particle size determination," *Physical Review*, vol. 56, no. 10, pp. 978–982, 1939.

[24] Z. Z. Zhang, F. Wang, K. Hu et al., "Improvement of resistive switching performance in sulfur-doped HfO_x-based RRAM," *Materials*, vol. 14, no. 12, article 3330, 2021.

[25] N. Ramshanker, K. L. Ganapathi, N. Varun, M. S. Bhat, and S. Mohan, "Development of CeO_2-HfO_2 Mixed oxide thin films for high performance oxygen sensors," *IEEE Sensors Journal*, vol. 21, no. 16, pp. 18326–18333, 2021.

[26] J. Shin, I. Kim, K. P. Biju et al., "TiO_2-based metal-insulator-metal selection device for bipolar resistive random access memory cross-point application," *Journal of Applied Physics*, vol. 109, no. 3, article 033712, 2011.

[27] A. Younis, D. Chu, and S. Li, "Oxygen level: the dominant of resistive switching characteristics in cerium oxide thin films," *Journal of Physics D-Applied Physics*, vol. 45, no. 35, p. 355101, 2012.

[28] C. Li, B. Zhang, Z. Qu et al., "Characterization of the inhomogeneity of Pt/CeO_x/Pt resistive switching devices prepared by magnetron sputtering," *Nanotechnology*, vol. 32, no. 14, p. 145710, 2021.

[29] Z. Qu, B. Zhang, C. Li et al., "A novel WOx-based memristor with a Ti nano-island array," *Electrochimica Acta*, vol. 377, p. 138123, 2021.

[30] Y. Li, Y. P. Zhong, J. J. Zhang et al., "Intrinsic memristance mechanism of crystalline stoichiometric $Ge_2Sb_2Te_5$," *Applied Physics Letters*, vol. 103, no. 4, article 043501, 2013.

[31] A. Tschope, C. Bauerle, and R. Birringer, "Numerical analysis of space charge layers and electrical conductivity in mesoscopic cerium oxide crystals," *Journal of Applied Physics*, vol. 95, no. 3, pp. 1203–1210, 2004.

[32] Y. M. Chiang, E. B. Lavik, and D. A. Blom, "Defect thermodynamics and electrical properties of nanocrystalline oxides: pure and doped CeO_2," *Nanostructured Materials*, vol. 9, no. 1-8, pp. 633–642, 1997.

[33] L. N. Liu, C. H. Zang, B. Wang et al., "Ceria thin film memristive device by magnetron sputtering method," *Vacuum*, vol. 173, p. 109128, 2020.

[34] D.-Y. Cho, M. Luebben, S. Wiefels, K.-S. Lee, and I. Valov, "Interfacial metal-oxide interactions in resistive switching memories," *ACS Applied Materials & Interfaces*, vol. 9, no. 22, pp. 19287–19295, 2017.

[35] A. Kindsmueller, A. Meledin, J. Mayer, R. Waser, and D. J. Wouters, "On the role of the metal oxide/reactive electrode interface during the forming procedure of valence change ReRAM devices," *Nanoscale*, vol. 11, no. 39, pp. 18201–18208, 2019.

[36] S. K. Nath, S. K. Nandi, S. Li, and R. G. Elliman, "Metal-oxide interface reactions and their effect on integrated resistive/threshold switching in NbO_x," *Nanotechnology*, vol. 31, no. 23, p. 235701, 2020.

[37] J. Park, E. Park, S.-G. Kim, D.-G. Jin, and H.-Y. Yu, "Analysis of the thermal degradation effect on a HfO_2-based memristor synapse caused by oxygen affinity of a top electrode metal and on a neuromorphic system," *ACS Applied Electronic Materials*, vol. 3, no. 12, pp. 5584–5591, 2021.

[38] H. A. Bafrani, M. Ebrahimi, S. B. Shouraki, and A. Z. Moshfegh, "A facile approach for reducing the working voltage of Au/TiO_2/Au nanostructured memristors by enhancing the local electric field," *Nanotechnology*, vol. 29, no. 1, article 015205, 2018.